

NIST Technical Note
NIST TN 2255

Physical Models and Dimensional Traceability of 2.4 mm Coaxial Airline Standards for Determining Systematic Uncertainties of Calibrated Scattering-Parameters

Jeffrey A. Jargon
Dylan F. Williams
Angela C. Stelson
Christian J. Long
Aaron M. Hagerstrom
John R. Stoup
Eric S. Stanfield
Wei Ren

This publication is available free of charge from:
<https://doi.org/10.6028/NIST.TN.2255>

NIST Technical Note
NIST TN 2255

Physical Models and Dimensional Traceability of 2.4 mm Coaxial Airline Standards for Determining Systematic Uncertainties of Calibrated Scattering-Parameters

Jeffrey A. Jargon
Dylan F. Williams
Angela C. Stelson
Christian J. Long
Aaron M. Hagerstrom
*RF Technology Division
Communications Technology Laboratory*

John R. Stoup
Eric S. Stanfield
Wei Ren
*Sensor Science Division
Physical Measurement Laboratory*

This publication is available free of charge from:
<https://doi.org/10.6028/NIST.TN.2255>

July 2023



U.S. Department of Commerce
Gina M. Raimondo, Secretary

National Institute of Standards and Technology
Laurie E. Locascio, NIST Director and Under Secretary of Commerce for Standards and Technology

NIST TN 2255
July 2023

Certain commercial equipment, instruments, software, or materials, commercial or non-commercial, are identified in this paper in order to specify the experimental procedure adequately. Such identification does not imply recommendation or endorsement of any product or service by NIST, nor does it imply that the materials or equipment identified are necessarily the best available for the purpose.

NIST Technical Series Policies

[Copyright, Use, and Licensing Statements](#)

[NIST Technical Series Publication Identifier Syntax](#)

Publication History

Approved by the NIST Editorial Review Board on 2023-07-05

How to Cite this NIST Technical Series Publication

Jargon JA, Williams DF, Stelson AC, Long CJ, Hagerstrom AM, Stoup JR, Stanfield ES, Ren W (2023) Physical Models and Dimensional Traceability of 2.4 mm Coaxial Airline Standards for Determining Systematic Uncertainties of Calibrated Scattering-Parameters. (National Institute of Standards and Technology, Boulder, CO), NIST Technical Note (TN) NIST TN 2255. <https://doi.org/10.6028/NIST.TN.2255>

NIST Author ORCID iDs

Jeffrey A. Jargon:	0000-0002-7897-6893
Dylan F. Williams:	0000-0002-8271-1505
Angela C. Stelson:	0000-0002-8900-140X
Christian J. Long:	0000-0002-4927-7209
Aaron M. Hagerstrom:	0000-0003-4675-4636
John R. Stoup:	0000-0003-3189-0889

Contact Information

jeffrey.jargon@nist.gov

Abstract

In this report, we document the models and dimensional traceability of our 2.4 mm coaxial airline standards for performing multiline thru-reflect-line calibrations up to 50 GHz using vector network analyzers. We identify the equations used in our models of the transmission-line standards and present a method for determining a coaxial line's metal conductivity using a closed-form solution relating it to the propagation constant. Next, we provide details of the traceable dimensional measurements and associated uncertainties of our 2.4 mm airline standards. And finally, we describe how our software, the NIST Microwave Uncertainty Framework, is used to implement physical models of calibration standards and propagate these systematic uncertainties to the calibrated scattering-parameters of a device under test. We include a measurement example for illustrative purposes.

Keywords

Calibration; coaxial airlines; dimensional traceability; measurement; models; standards; systematic uncertainties; vector network analyzer.

Table of Contents

1. Introduction.....	1
2. Transmission-Line Model.....	2
3. Metal Conductivity.....	5
4. Connector Interface.....	6
5. Dimensional Measurements.....	11
6. Software Implementation.....	15
7. Conclusions.....	23
References.....	23

List of Tables

Table 1. Inner conductor diameter (d) measurements of airlines.....	13
Table 2. Outer conductor diameter (D) measurements of airlines.....	14
Table 3. Inner conductor length (l) measurements of airlines.....	14
Table 4. Outer conductor length (L) measurements of airlines.....	14
Table 5. Differences between outer and inner conductor length (Δ_l) measurements of airlines.....	15

List of Figures

Fig. 1. Cross-section of a coaxial transmission line. Propagation is in the positive z direction (coming out of the page).	2
Fig. 2. Longitudinal cross section of a coaxial connector interface.....	7
Fig. 3. Airline connected to two-port VNA has a gap at each port.	8
Fig. 4. Transforming the S -matrix of an airline to a $50\ \Omega$ reference impedance.....	9
Fig. 5. MUF 'Model' file of coaxial transmission-line standard (S/N A003) with correlated pin-depth gaps. Note that the 'Length' parameter does not show a corresponding value since it is represented by a 'Sum of Parameters' file.....	17
Fig. 6. MUF 'Parameter' file of transmission-line standard's inner conductor diameter (S/N A003).	18
Fig. 7. MUF 'Sum of Parameters' file of transmission-line standard's length (S/N A003).....	18
Fig. 8. MUF 'VNA Uncertainty Calculator' showing definitions, types, and measurement files.....	18
Fig. 9. Real part of $\epsilon_{r,\text{eff}}$ obtained from the multiline TRL calibration.....	20
Fig. 10. Imaginary part of $\epsilon_{r,\text{eff}}$ obtained from the multiline TRL calibration.	20
Fig. 11. Metal conductivity σ calculated using equations in Section 3.	21
Fig. 12. Measured and modeled values ($\sigma = 8.9 \times 10^6\ \text{S/m}$ and $\sigma = 4.2 \times 10^7 \pm 0.3 \times 10^7\ \text{S/m}$) of $ S_{21} $ as a function of frequency for airline (S/N A681).....	21
Fig. 13. Measured (with 95 % confidence interval dashed lines) and modeled values ($\sigma = 4.2 \times 10^7 \pm 0.3 \times 10^7\ \text{S/m}$) of $ S_{21} $ as a function of frequency for airline (S/N A681).	22
Fig. 14. Measured (with 95 % confidence interval dashed lines) of $ S_{11} $ as a function of frequency for airline (S/N A681).	22
Fig. 15. Values of $ S_{21} $ as a function of frequency along with its 95 % confidence intervals for the calibrated 20 dB attenuator check standard (S/N C24201) compared to a previous measurement along with its traditional confidence intervals.	23

Acknowledgments

The authors thank Ari Feldman, Dazhen Gu, Paul Hale, Mitch Wallis, and Brian Washburn for their helpful comments.

1. Introduction

The mission of the National Institute of Standards and Technology (NIST) is to promote U.S. innovation and industrial competitiveness by advancing measurement science, standards, and technology in ways that enhance economic security and improve our quality of life [1]. To help meet the needs of the nation, NIST provides numerous measurement services that assist customers in establishing metrological traceability to fundamental constants. Such traceability requires an unbroken chain of measurements and uncertainties for each link in the chain [2].

One such measurement service provided by NIST is microwave scattering-parameters (Service ID 61290S) [3]. Scattering-parameters (S -parameters) describe the behavior of linear networks when undergoing sinusoidal electrical stimuli. Customers may send in one- and two-port artifacts with a variety of coaxial or rectangular waveguide connectors, and NIST provides measurements at user-selected frequencies appropriate for the connector type by using a vector network analyzer (VNA) characterized with traceable calibration artifacts.

Although numerous calibration techniques for VNAs are available, multiline thru-reflect-line (TRL) is perhaps the most fundamental and accurate method [4, 5]. Multiline TRL utilizes an ensemble of uncorrected two-port S -parameter measurements with switch terms [6] or complex forward and backward wave-parameters [7] collected from a set of calibration artifacts. These measurements are used to compute correction coefficients. These coefficients can then be used to correct the measured S -parameters or wave-parameters of a device under test (DUT). While it is more common to simply correct S -parameters, the wave-parameters are more general and allow for modulated and large-signal measurements to be supported by the calibration.

Multiline TRL is based on transmission-line standards that differ only in length and an arbitrary reflect standard that is identical for both port connections. Making use of multiple transmission-line standards enables redundancy for the suppression of random errors and permits calibration over a wide frequency band. Furthermore, multiline TRL determines the propagation constant of the line standards. This can facilitate determining the frequency-dependent characteristic impedance and transforming the calibration's reference impedance to a desired reference impedance, such as the impedance of an ideal guide [5, 8].

S -parameters are, by definition, unitless quantities defined by ratios of the wave-parameters. The wave-parameters are determined through magnitude and phase readings, and are ratioed, necessitating linearity in the measurement system. The traceability path for corrected S -parameters depends on the calibration method. In the case of multiline TRL, S -parameters are traceable to dimensions of the transmission-line standards, namely each line's length and cross-sectional geometry. For coaxial standards, the cross-sectional dimensions of interest are the outer conductors' inner diameters and the inner conductors' outer diameters. In particular, the ratio of the inner diameter of the outer conductor to the outer diameter of the inner conductor is used to determine the characteristic impedance of coaxial transmission lines.

Here, we document the models and dimensional traceability of our 2.4 mm coaxial airline standards used for performing multiline TRL calibrations. The 2.4 mm designation refers to a size that is specified to have an outer-conductor inside diameter D of 2.4 mm and an inner-conductor

outside diameter d of 1.0423 mm, with a specified upper-rated frequency of 50 GHz [9]. In Section 2, we provide the equations used in our model of the transmission-line standards. These models are used for determining systematic uncertainties of each standard and serve as the basis for propagating them through the calibration algorithm to the calibrated S -parameters of a DUT. In Section 3, we present a method for determining the coaxial airline's metal conductivity using a closed-form solution relating it to the propagation constant. In Section 4, we review the equations used to account for gap impedances between two airlines when they are joined, such as when a transmission line is connected to a test port of a VNA. In Section 5, we provide details of the traceable dimensional measurements and associated uncertainties of our 2.4 mm airline standards. And in Section 6, we describe how our software, the NIST Microwave Uncertainty Framework [10], is used to implement physical models of calibration standards and automatically propagate the uncertainties to the calibrated S -parameters of a DUT. We include an example to illustrate our entire process of providing traceable measurements.

2. Transmission-Line Model

A coaxial line consists of concentric conductors, where a single, inner transmission line is surrounded by a conductive, ground shield. The upper frequency limit of the single-mode electromagnetic wave propagation is limited by the line's dimensions, specifically the inner-conductor outside diameter d and the outer-conductor inside diameter D , as shown in Fig. 1.

Coaxial transmission lines offer advantages over rectangular waveguide in that they offer a much higher bandwidth of single-mode propagation and can pass direct currents (DC) along with radiofrequency (RF) signals. Disadvantages of coaxial lines include higher loss and less shielding than rectangular waveguide.

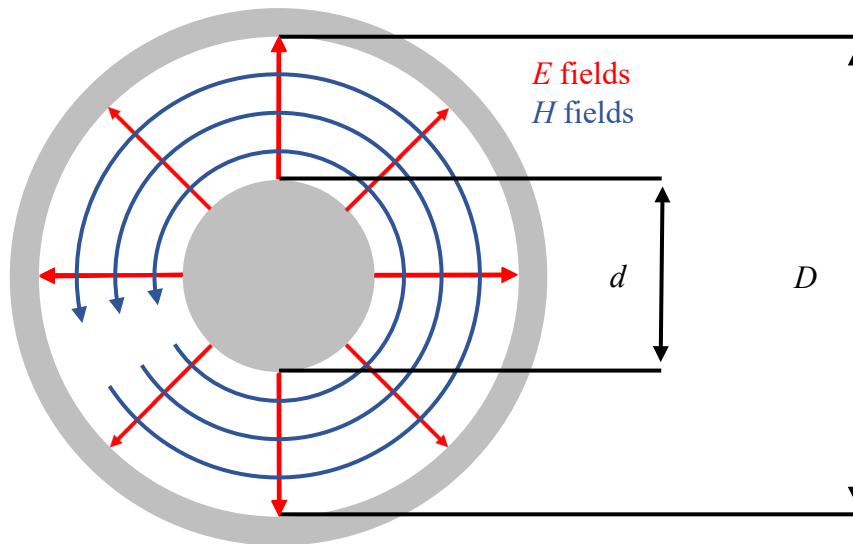


Fig. 1. Cross-section of a coaxial transmission line. Propagation is in the positive z direction (coming out of the page).

Because coaxial transmission lines consist of two conductors, they support the transverse electromagnetic (TEM) mode, where electric E and magnetic H fields on the line are transverse to the direction of propagation. An important property of TEM waves is that the E and H fields are uniquely related to the voltage V and current I , respectively. Since the TEM mode has no lower cutoff-frequency, coaxial lines can transmit frequencies all the way down to DC. The second-lowest mode in coaxial lines is the transverse electric TE_{11} mode. The cutoff frequency of this mode represents the maximum frequency of TEM-only propagation [11], and is given by

$$f_{c,11} \approx \frac{2c}{\pi(D+d)\sqrt{\epsilon_r}}, \quad (2.1)$$

where $c = 2.99792458 \times 10^8$ m/s is the speed of light in vacuum and ϵ_r is the relative permittivity of the dielectric material filling the gap between the center and outer conductors. Connectors may have a lower cutoff frequency, which often limit the maximum frequency.

In this section, we summarize the various equations used for modeling the S -parameters of a coaxial transmission line with an air dielectric (airline). The S -parameters are directly a function of the propagation constant γ and the line length l . The complex-valued propagation constant is dependent on the phase velocity v , the metal conductivity σ , and the characteristic impedance Z_{00} of the TEM mode in the line, which is, in turn, dependent on the loss tangent ($\tan \delta_l$) of the dielectric material, the relative permittivity ϵ_r of the material, and the dimensions d and D .

Consider a coaxial airline with inner and outer conductor diameters d and D , respectively. Assuming both conductors have infinite conductivity, and there is an eccentricity due to the center of the inner conductor being offset from the center of the outer conductor by a distance e , the characteristic impedance of the transverse electromagnetic (TEM) mode in the line Z_{00} [12, 13] is given by

$$Z_{00} = \frac{\eta}{2\pi} \ln \left[\frac{d^2 + D^2 - 4e^2 + \sqrt{(D^2 - d^2 + 4e^2)^2 - (4De)^2}}{2dD} \right]. \quad (2.2)$$

The eccentricity e is defined as the offset distance of the center of the inner conductor from the center of the outer conductor. The wave impedance η in a nonmagnetic, lossy dielectric material is

$$\eta = \sqrt{\frac{\mu_0}{\epsilon}}, \quad (2.3)$$

where $\mu_0 = 1.25663706212 \times 10^{-6}$ H/m is the permeability of free space [14] and ϵ is the complex permittivity of the material, commonly expressed as

$$\epsilon = \epsilon' - j\epsilon''. \quad (2.4)$$

The loss tangent ($\tan \delta_l$) of a dielectric material is defined as

$$\tan \delta_l = \frac{\omega \varepsilon'' + \sigma_\varepsilon}{\omega \varepsilon'}, \quad (2.5)$$

where σ_ε is the finite conductivity of the material, $\omega = 2\pi f$ is the radial frequency, and f is the frequency in Hz. At microwave frequencies, the $\omega \varepsilon''$ term is usually much larger than σ_ε due to the high value of ω , and thus

$$\tan \delta_l \approx \frac{\varepsilon''}{\varepsilon'}. \quad (2.6)$$

Equation (2.4) may then be expressed

$$\varepsilon = \varepsilon' (1 - j \tan \delta_l). \quad (2.7)$$

The real part of the permittivity is often expressed as

$$\varepsilon' = \varepsilon_r \varepsilon_0, \quad (2.8)$$

where ε_r is the relative permittivity of the material and ε_0 is the permittivity of free space [15]. Thus, the wave impedance in Eq. (2.3) may be written as

$$\eta = \sqrt{\frac{\mu_0}{\varepsilon_r \varepsilon_0 (1 - j \tan \delta_l)}}. \quad (2.9)$$

The phase velocity v (m/s) in a nonmagnetic, lossy dielectric material is

$$v = \frac{1}{\sqrt{\varepsilon \mu_0}}. \quad (2.10)$$

Substituting Eq. (2.7) and Eq. (2.8) into Eq. (2.10) gives

$$v = \frac{1}{\sqrt{\varepsilon_r \varepsilon_0 (1 - j \tan \delta_l) \mu_0}}. \quad (2.11)$$

For a coaxial airline with losses dominated by conductor loss [16, 17], the characteristic impedance Z_0 (Ω) and propagation constant γ (1/m) of the quasi-TEM mode are given as

$$Z_0 = Z_{00} \sqrt{1 + (1 - j) \frac{v R_c}{\omega Z_{00}}} \quad (2.12)$$

and

$$\gamma = j \frac{\omega}{v} \sqrt{1 + (1 - j) \frac{v R_c}{\omega Z_{00}}}. \quad (2.13)$$

The conductor resistance per-unit-length R_c (Ω/m) [16, 17] is given by

$$R_c = \frac{1}{\sigma \delta} \left(\frac{1}{\pi \rho_D D} + \frac{1}{\pi \rho_d d} \right), \quad (2.14)$$

where σ is the metal conductivity (S/m), δ is the skin depth (m) given by

$$\delta = \sqrt{\frac{2}{\omega \mu_0 \sigma}}, \quad (2.15)$$

and ρ_d and ρ_D are defined as

$$\rho_d = \frac{D^2 - d^2 - 4e^2}{\sqrt{[D^2 - (d + 2e)^2][D^2 - (d - 2e)^2]}} \quad (2.16)$$

and

$$\rho_D = \frac{D^2 - d^2 + 4e^2}{\sqrt{[(D + 2e)^2 - d^2][(D - 2e)^2 - d^2]}}. \quad (2.17)$$

For a coaxial section of airline having length l (m), the transmission coefficients ($S_{21} = S_{12}$) represent the ratios of the complex amplitude of the wave at the end of the airline to the complex amplitude at the beginning of the airline, and are given by

$$S_{21} = S_{12} = e^{-\gamma l}. \quad (2.18)$$

An ideal coaxial section of line is defined to have reflection coefficients ($S_{11} = S_{22}$) of zero.

From the equations presented in this section, we see that the model of a coaxial section of line requires the following variables: frequency f , length l , inner conductor diameter d , outer conductor diameter D , eccentricity e , relative permittivity ϵ_r , loss tangent ($\tan \delta_l$), and metal conductivity σ .

3. Metal Conductivity

From the previous section, we see that one of the inputs required for the model of a coaxial airline is the metal conductivity σ . This value can be determined experimentally using a closed-form solution relating the propagation constant to the conductivity and taking the mean value over the measured frequencies. Assuming the conductivity for all of the lines is the same for a single kit from a given manufacturer, we first perform a multiline TRL calibration [4], which calculates the

frequency-dependent values for the effective relative permittivity $\epsilon_{r,\text{eff}}$. This quantity is defined as [5]:

$$\epsilon_{r,\text{eff}} = -\left(\frac{c\gamma}{\omega}\right)^2. \quad (3.1)$$

Solving for the propagation constant γ gives

$$\gamma = \sqrt{-\epsilon_{r,\text{eff}}}\left(\frac{\omega}{c}\right). \quad (3.2)$$

Here, it is important to check the sign of γ to make sure the root choice is correct. For passive devices, the real part, corresponding to the attenuation constant, should be positive so that energy is not created. The attenuation constant α is thus given by

$$\alpha = \text{Re}\{\gamma\}. \quad (3.3)$$

To first-order approximation at high frequencies, the metal conductivity σ is related to the attenuation constant α as follows [18]:

$$\sigma \approx \left[\frac{1 + (D/d)}{100\alpha D}\right]^2 \frac{\mu_0 f}{\pi}. \quad (3.4)$$

Equation (3.4) can be derived from Eqs. (2.13) and (2.14). The values of σ calculated at each of the measured frequencies may be used to determine a mean value and a standard deviation.

This simple approximation does not account for nonidealities in the airlines, such as surface roughness, residual machining stresses, and multiple layers of metal. Thus, another technique for determining metal conductivity is to simply iterate on the parameter in the model until it agrees with measured results. These two methods are examined further in Section 6.

4. Connector Interface

A common assumption made in VNA calibrations, including multiline TRL, is that the connector interface at the test ports is identical for all calibration standards. In practice, this assumption is incorrect. Aside from connector repeatability, there are variations in the inner conductor gap g due to dimensional tolerances of the connectors (i.e., pin diameter d_p and pin depth l_p) and eccentricity e . The inner conductor gap is illustrated in Fig. 2, which shows a simplified longitudinal cross-section of a male connector on the right mating with a female connector on the left.

By design, both the male and female inner conductors are set back small distances from the outer conductor mating planes, known as pin depths, to ensure undamaged connections. Thus, an inner conductor gap is unavoidable. The resulting gap g creates a small discontinuity, causing an impedance mismatch. The inductive impedance of the gap [11, 19] can be approximated by

$$Z_g \approx j \frac{\mu_0}{2\pi} \omega g \ln \left(\frac{d}{d_p} \right). \quad (4.1)$$

For an airline connected to a two-port VNA, there will be two gaps, g_1 and g_2 , as illustrated in Fig. 3. It is possible to account for the impedance mismatches assuming correlated pin-depth gaps. To do so, we begin by defining the total inner conductor gap g_T as the sum of the two ports' pin depths (l_{p1} and l_{p2}) and the difference between the lengths of the outer and inner conductor lengths Δ_l of the airline:

$$g_T = \Delta_l + l_{p1} + l_{p2}. \quad (4.2)$$

The total gap can be distributed between ports 1 and 2 using the following expressions:

$$g_1 = \frac{g_T(1 - l_r)}{2} \quad (4.3)$$

and

$$g_2 = \frac{g_T(1 + l_r)}{2}, \quad (4.4)$$

where l_r is the relative inner conductor position and can have values ranging from -1 to +1. If l_r is +1, the entire gap g_T is located at port 2; if l_r is -1, the entire gap g_T is located at port 1; and if l_r is zero, the gap is split evenly between the two ports.

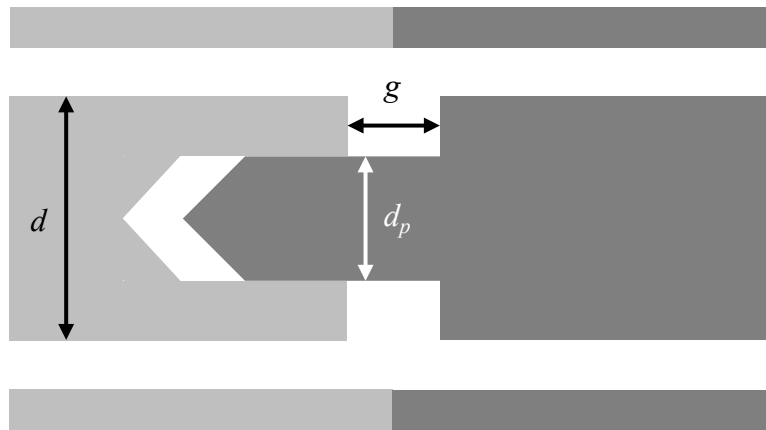


Fig. 2. Longitudinal cross section of a coaxial connector interface.



Fig. 3. Airline connected to two-port VNA has a gap at each port.

Referring to Eq. (4.1), the inductive gap impedance Z_{g1} at port 1 is given by

$$Z_{g1} = j \frac{\mu_0}{2\pi} \omega g_1 \ln \left(\frac{d}{d_{p1}} \right). \quad (4.5)$$

The S -matrix \mathbf{S}_{g1} corresponding to the port 1 gap impedance is given by the transformation [20]:

$$\mathbf{S}_{g1} = \frac{1}{Z'_{g1} + 2} \begin{bmatrix} Z'_{g1} & 2 \\ 2 & Z'_{g1} \end{bmatrix}, \quad (4.6)$$

where

$$Z'_{g1} = \frac{Z_{g1}}{50}. \quad (4.7)$$

Eq. (4.7) ensures the S -parameters correspond to a 50Ω reference impedance.

Referring to Eq. (4.1) again, the inductive gap impedance Z_{g2} at port 2 is given by

$$Z_{g2} = j \frac{\mu_0}{2\pi} \omega g_2 \ln \left(\frac{d}{d_{p2}} \right). \quad (4.8)$$

In a similar fashion to Eqs. (4.6) and (4.7), the S -matrix \mathbf{S}_{g2} corresponding to the port 2 gap impedance is given by

$$\mathbf{S}_{g2} = \frac{1}{Z'_{g2} + 2} \begin{bmatrix} Z'_{g2} & 2 \\ 2 & Z'_{g2} \end{bmatrix}, \quad (4.9)$$

where

$$Z'_{g2} = \frac{Z_{g2}}{50}. \quad (4.10)$$

The overall S -matrix \mathbf{S} of the airline with gaps on both ports is calculated by first cascading the S -matrix of the of the port 1 gap \mathbf{S}_{g1} (Eq. (4.6)) with the S -matrix of the airline \mathbf{S}_A , and then cascading

that result with the S -matrix of the port 2 gap \mathbf{S}_{g2} (Eq. (4.9)), where all the S -parameters correspond to a reference impedance of 50Ω :

$$\mathbf{S} = (\mathbf{S}_{g1} \times \mathbf{S}_A) \times \mathbf{S}_{g2}. \quad (4.11)$$

Here the symbol ‘ \times ’ refers to the cascade of S -matrices rather than a simple multiplication. This implies a transformation from S -matrices to T -matrices prior to the multiplication.

The S -matrix of the airline \mathbf{S}_A must also be transformed to a 50Ω reference impedance, as shown in Fig. 4a, where the airline has length l and characteristic impedance Z_0 . Equations (4.12)-(4.23) enable this transformation while simultaneously allowing for different values of eccentricity at the two ports (e_1 and e_2) by treating the two halves of the airline separately, as shown in Fig. 4b. The left half of the airline has length $l/2$ and characteristic impedance Z_{01} and the right half has length $l/2$ and characteristic impedance Z_{02} .

We begin with the widely known relationship for calculating the reflection coefficient Γ of a load impedance Z_L with respect to a reference impedance Z_{ref} , which is given as

$$\Gamma = \frac{Z_L - Z_{\text{ref}}}{Z_L + Z_{\text{ref}}}. \quad (4.12)$$

The reflection coefficient at port 1 looking toward that half of the airline is given by

$$\Gamma_1 = \frac{Z_{01} - 50}{Z_{01} + 50}. \quad (4.13)$$

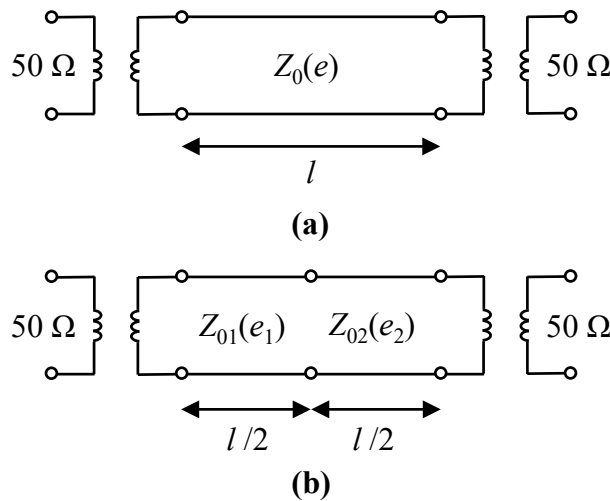


Fig. 4. Transforming the S -matrix of an airline to a 50Ω reference impedance.

The S -matrix of the impedance transformer on the port 1 side of the left half of the airline $\mathbf{S}_{1,1}$ is given by

$$\mathbf{S}_{1,1} = \begin{bmatrix} \Gamma_1 & \sqrt{1 - \Gamma_1^2} \\ \sqrt{1 - \Gamma_1^2} & -\Gamma_1 \end{bmatrix} \quad (4.14)$$

and the S -matrix of the impedance transformer on the port 2 side of the left half of the airline $\mathbf{S}_{2,1}$ is given by

$$\mathbf{S}_{2,1} = \begin{bmatrix} -\Gamma_1 & \sqrt{1 - \Gamma_1^2} \\ \sqrt{1 - \Gamma_1^2} & \Gamma_1 \end{bmatrix}. \quad (4.15)$$

The S -matrix of the left half of the airline \mathbf{S}_{γ_1} is given by

$$\mathbf{S}_{\gamma_1} = \begin{bmatrix} 0 & e^{-\gamma_1 l/2} \\ e^{-\gamma_1 l/2} & 0 \end{bmatrix}, \quad (4.16)$$

where γ_1 is the propagation constant of the left half of the airline. The overall S -matrix of the left half of the airline \mathbf{S}_1 transformed to a 50 Ω reference impedance is calculated by concatenating Eq. (4.14) and Eq. (4.16), and then concatenating that result with the Eq. (4.15):

$$\mathbf{S}_1 = (\mathbf{S}_{1,1} \times \mathbf{S}_{\gamma_1}) \times \mathbf{S}_{2,1}. \quad (4.17)$$

The reflection coefficient at port 2 looking toward that half of the airline is given by

$$\Gamma_2 = \frac{Z_{02} - 50}{Z_{02} + 50}. \quad (4.18)$$

The S -matrix of the impedance transformer on the port 1 side of the right half of the airline $\mathbf{S}_{1,2}$ is given by

$$\mathbf{S}_{1,2} = \begin{bmatrix} \Gamma_2 & \sqrt{1 - \Gamma_2^2} \\ \sqrt{1 - \Gamma_2^2} & -\Gamma_2 \end{bmatrix} \quad (4.19)$$

and the S -matrix of the impedance transformer on the port 2 side of the right half of the airline $\mathbf{S}_{2,2}$ is given by

$$\mathbf{S}_{2,2} = \begin{bmatrix} -\Gamma_2 & \sqrt{1 - \Gamma_2^2} \\ \sqrt{1 - \Gamma_2^2} & \Gamma_2 \end{bmatrix}. \quad (4.20)$$

The S -matrix of the right half of the airline \mathbf{S}_{γ_2} is given by

$$\mathbf{S}_{\gamma_2} = \begin{bmatrix} 0 & e^{-\gamma_2 l/2} \\ e^{-\gamma_2 l/2} & 0 \end{bmatrix}, \quad (4.21)$$

where γ_2 is the propagation constant of the right half of the airline. The overall S -matrix of the right half of the airline \mathbf{S}_2 transformed to a 50 Ω reference impedance is calculated by cascading Eq. (4.19) and Eq. (4.21), and then concatenating that result with the Eq. (4.20):

$$\mathbf{S}_2 = (\mathbf{S}_{1,2} \times \mathbf{S}_{\gamma_2}) \times \mathbf{S}_{2,2}. \quad (4.22)$$

The S -matrix of the entire airline \mathbf{S}_A is determined by concatenating Eq. (4.17) and Eq. (4.22):

$$\mathbf{S}_A = \mathbf{S}_1 \times \mathbf{S}_2. \quad (4.23)$$

Eq. (4.23) is plugged into Eq. (4.11) to calculate the overall S -matrix \mathbf{S} of the airline with gaps on both ports.

From the equations presented in the previous section and this one, we see that the model of a coaxial section of line with correlated pin-depth gaps requires the following inputs: frequency f , length l , inner conductor diameter d , outer conductor diameter D , relative permittivity ϵ_r , loss tangent ($\tan \delta_l$), metal conductivity σ , eccentricity at both ports e_1 and e_2 , pin diameters at both ports d_{p1} and d_{p2} , pin depths at both ports l_{p1} and l_{p2} , the difference between the lengths of the outer and inner conductor lengths Δl , and the relative inner conductor position l_r .

5. Dimensional Measurements

Our 2.4 mm calibration kit, manufactured by Maury Microwave Corporation¹, consists of eleven airlines with lengths ranging from 25.00619 mm to 74.98632 mm, which are used for multiline TRL calibrations. The inner and outer conductors were measured by the NIST Dimensional Metrology Group in Gaithersburg, MD [21].

The inner conductor diameters (d) were measured using a contact micrometer combined with a laser displacement interferometer. The process employed a traceable, stabilized HeNe laser as the length standard. NIST control standards were present throughout the measurement to maintain process control and develop statistical long-term reproducibility data for the measurement system. Each artifact was measured multiple times to generate short-term repeatability data and to characterize variations in two-point diameter measurements. The statistical data provided

¹ Certain equipment, instruments, software, or materials, commercial or non-commercial, are identified in this paper in order to specify the experimental procedure adequately. Such identification is not intended to imply recommendation or endorsement of any product or service by NIST, nor is it intended to imply that the materials or equipment identified are necessarily the best available for the purpose.

continuous measurement assurance of the process. The average, undeformed, measured diameter of each conductor was reported at defined positions along the axis of the conductor. The conductors were positioned using a precision stage and a frictionless air pad to maintain proper orientation during data collection. Each conductor was rotated several times to sample the geometrical form around the pin.

The outer conductor diameters (D) were measured using a coordinate measuring machine (CMM) error-mapped with a traceable stabilized HeNe laser system. The CMM was housed in a constant humidity measurement environment where room temperature was controlled to 20.00 ± 0.03 ° C. The measurement process employed several parts. The artifacts were measured multiple times to generate short-term repeatability data and to sample artifact geometry and surface finish effects. NIST control standards were measured concurrently to develop statistical long-term reproducibility data for the measurement system. The outer conductors were fixtured using small traces of epoxy to prevent movement during the gauging process. No restrictive or clamping devices were used. The features of interest were measured using multiple applied forces and the results extrapolated to zero force to address any fixturing, surface quality, or elastic deformation concerns.

The standard uncertainty for the inner diameters d measurements was specified to be 0.125 μm . Table 1 lists the measured values of the inner diameters along with uncertainties. The standard uncertainty for the outer diameters D measurements was specified to be 0.105 μm . Table 2 lists the measured values of the outer diameters along with uncertainties.

Rather than tracking each of the devices' individual measurements, we used the specified values of 1.0423 mm for the inner diameter and 2.4000 mm for the outer diameter, and then determined the uncertainties by calculating the root-mean-squares (RMS) of the diameters from the measured values listed in Tables 1 and 2. This resulted in standard uncertainties of ± 0.0016 mm for the inner diameters and ± 0.0006 mm for the outer diameters.

We chose to use the specified values of inner and outer diameters for all the airlines as opposed to the individually measured values because the multiline TRL algorithm is not compatible with individually measured inner and outer diameters. The multiline TRL algorithm is considered the most accurate calibration algorithm because the self-defined models it employs do not rely on approximate analytic expressions for the S -parameters of the airlines, but rather only on measured S -parameters and lengths of the airlines. This is a subtle point – multiline TRL does not use any other parameters or error mechanisms to determine the nominal calibration, rather they are only used for determining uncertainties.

The inner conductor lengths (l) were measured using a commercial vision instrument with variable magnification and image illumination capability. Each end of the inner conductors was imaged independently, rotated in its fixture, and the through the lens illumination was stepped through several levels to negate the effects of contaminants, reflection, and edge detection bias at the inner conductor shoulder positions. A master cylinder of similar size was calibrated for shoulder-to-shoulder length and provided a control length for the measurements. The data at five different illumination levels were averaged to obtain the results. The standard uncertainty for this radius data was estimated to be about 1.0 μm based on the reproducible performance of the inner

conductors and the control cylinder. Table 3 lists the measured values of length along with uncertainty for the eleven airlines, as designated by serial number.

The outer conductor lengths (L) were determined by measuring two concentric circular planes on the flat bore shoulders at each end of the respective conductor. The CMM was mastered using a calibrated gauge block mounted in the same orientation and data was collected in the same manner. The two end plane datasets were collected at radii of 1.45 mm and 1.60 mm from the bore center axis. As these shoulders were used for hard end locations during assembly of the devices, the longest measured length most closely approximates the assembled conductor length. Most of the conductors' length measurements at the two locations were consistent to better than 0.2 μm . The standard uncertainty of the outer conductor length was estimated to be 0.25 μm . However, outer conductors A005, A006, A679, and A684 indicated some end plane damage at one of the surfaces, so these conductors have an elevated standard uncertainty of 0.75 μm . Table 4 lists the measured values of length along with uncertainty for the eleven airlines, as designated by serial number.

In Eq. (4.2), we defined the total inner conductor gap g_T as the sum of the two ports' pin depths (l_{p1} and l_{p2}) and the difference between the lengths of the outer and inner conductor lengths Δ_l of the airline, thus we compute Δ_l for each airline in Table 5. The standard uncertainties are calculated from the RMS respective values of the outer and inner uncertainties.

Since dimensional measurements were not made on the airlines' pin depths and pin diameters, we relied on values and uncertainties specified in the Institute of Electrical and Electronics Engineers (IEEE) Standard 287 [8]. The maximum allowable pin depth for 2.4 mm laboratory precision connectors (LPC) is 0.013 mm. Thus, we specified the pin depths of our airlines to be 0.0065 mm \pm 0.0065 mm. Furthermore, the standard specifies the pin diameters d_p to be 0.511 mm \pm 0.005 mm.

Table 1. Inner conductor diameter (d) measurements of airlines.

Serial Number	Diameter \pm Std. Unc. (mm)
A003	1.04120 \pm 0.000125
A004	1.04046 \pm 0.000125
A005	1.04079 \pm 0.000125
A006	1.04183 \pm 0.000125
A007	1.03943 \pm 0.000125
A008	1.04083 \pm 0.000125
A675	1.04356 \pm 0.000125
A677	1.04026 \pm 0.000125
A679	1.04130 \pm 0.000125
A681	1.04121 \pm 0.000125
A684	1.04064 \pm 0.000125

Table 2. Outer conductor diameter (D) measurements of airlines.

Serial Number	Diameter \pm Std. Unc. (mm)
A003	2.39984 \pm 0.000105
A004	2.39877 \pm 0.000105
A005	2.39963 \pm 0.000105
A006	2.39938 \pm 0.000105
A007	2.39968 \pm 0.000105
A008	2.40017 \pm 0.000105
A675	2.40037 \pm 0.000105
A677	2.39981 \pm 0.000105
A679	2.40025 \pm 0.000105
A681	2.40077 \pm 0.000105
A684	2.40028 \pm 0.000105

Table 3. Inner conductor length (l) measurements of airlines.

Serial Number	Length \pm Std. Unc. (mm)
A003	25.00066 \pm 0.00100
A004	26.97991 \pm 0.00100
A005	28.97630 \pm 0.00100
A006	74.93220 \pm 0.00100
A007	30.96012 \pm 0.00100
A008	32.99391 \pm 0.00100
A675	27.00806 \pm 0.00100
A677	29.00321 \pm 0.00100
A679	30.00021 \pm 0.00100
A681	34.98194 \pm 0.00100
A684	74.98710 \pm 0.00100

Table 4. Outer conductor length (L) measurements of airlines.

Serial Number	Length \pm Std. Unc. (mm)
A003	25.00619 \pm 0.00025
A004	26.98835 \pm 0.00025
A005	28.99361 \pm 0.00075
A006	74.95649 \pm 0.00075
A007	30.97264 \pm 0.00025
A008	32.99411 \pm 0.00025
A675	26.99082 \pm 0.00025
A677	28.99964 \pm 0.00025
A679	29.99915 \pm 0.00075
A681	34.99074 \pm 0.00025
A684	74.98632 \pm 0.00075

Table 5. Differences between outer and inner conductor length (Δ_l) measurements of airlines.

Serial Number	Length Difference \pm Std. Unc. (mm)
A003	0.00553 \pm 0.00103
A004	0.00844 \pm 0.00103
A005	0.01731 \pm 0.00125
A006	0.02429 \pm 0.00125
A007	0.01252 \pm 0.00103
A008	0.00020 \pm 0.00103
A675	-0.01724 \pm 0.00103
A677	-0.00357 \pm 0.00103
A679	-0.00106 \pm 0.00125
A681	0.00880 \pm 0.00103
A684	-0.00078 \pm 0.00125

6. Software Implementation

We utilized the NIST Microwave Uncertainty Framework (MUF) [10, 22-24] to develop physical models of our multiline-TRL, 2.4 mm coaxial calibration kit. The MUF provides parallel sensitivity and Monte-Carlo analyses and enables us to capture and propagate the significant S -parameter measurement uncertainties and statistical correlations between them [24]. By identifying and modeling the physical error mechanisms in the calibration standards, as we did in the previous sections, we can determine the systematic uncertainties in S -parameters, including their cross-frequency correlations. These uncertainties can then be propagated to measurements of the DUTs.

Figure 5 illustrates an example of how model-building is accomplished in the MUF. By bringing up the ‘Model’ program, the user is offered numerous choices. The top-most pull-down menu is labeled ‘Model Category,’ which includes ‘Coaxial transmission lines.’ With this option chosen, the next pull-down menu, entitled ‘Selection,’ offers a variety of waveguide models including ‘Coaxial transmission line with correlated pin-depth gaps (alternate formulation).’ This model implements the equations we presented in Sections 2 and 4. Immediately below the ‘Selection’ menu is a field called ‘Name,’ where the user may enter a descriptive title. And following that is a list of input mechanisms required for the chosen model. In the case we’re illustrating, we need to enter parameters files for the airline’s inner-conductor diameter (d), outer-conductor diameter (D), outer-conductor length (L), relative dielectric constant ($\epsilon_{r,eff}$), dielectric loss tangent ($\tan \delta_l$), metal conductivity (σ), eccentricities at ports 1 and 2 (e_1 and e_2), pin diameters at ports 1 and 2 (d_{p1} and d_{p2}), pin depths at ports 1 and 2 (l_{p1} and l_{p2}), outer-conductor minus inner-conductor length (Δ_l), and relative inner-conductor position (p_r).

The mechanism values shown in Fig. 5 correspond to a 25.00619 mm airline (S/N A003). For each mechanism, a ‘Parameter’ file is required that contains a descriptive title, a mean value of the parameter and the probability-distribution limits of the parameter, as illustrated in Fig. 6. Once all the ‘Parameter’ files are created for a given standard, they can be dragged and dropped into the appropriate parameters in the ‘Model’ program, where the directory information and mean values

are displayed. This model can then be saved and used as the standard definition or cascaded with additional models.

Since the dimensions of our devices were measured at a temperature of 20 ° C and the temperature in our *S*-parameter laboratory is specified to be 23 ± 2 ° C, we took thermal expansion into account in determining the lengths of our beryllium copper airlines. BeCu has a linear thermal expansion coefficient (α_L) of approximately 19×10^{-6} (° C)⁻¹ [25]. We modified the length of each airline as

$$l_{\Delta T} = l(1 + \alpha_L \Delta T), \quad (6.1)$$

where l is the length of the shim measured at 20 ° C, ΔT is the difference in temperature (in our case 3 ± 2 ° C), and $l_{\Delta T}$ is the resulting length of the airline in our laboratory. Equation (6.1) can be realized in the MUF by utilizing a ‘Sum of Parameters’ file, as illustrated in Fig. 7. Parameters for the temperatures, measured line length, and thermal expansion coefficient are dragged and dropped into the ‘List of Parameters’ and the equation is entered into the area designated, ‘Expression to be evaluated,’ where the parameter names are contained in curly brackets. The resulting ‘Sum of Parameters’ file can be dragged and dropped into a ‘Model’ just like a ‘Parameter’ file.

As described in Section 3, the first step in determining the metal conductivity σ is to perform a multiline TRL calibration, which will provide us with frequency-dependent values for the effective relative permittivity $\epsilon_{r,\text{eff}}$. The multiline TRL calibration is set up using the ‘VNA Uncertainty Calculator’ program in the MUF, as shown in Fig. 8. The pull-down menu labeled ‘Main calibration’ allows the user to set up the standards to be used in the calibration. The first column labeled ‘Definition’ is the area where the ‘Model’ or ‘Cascade’ files for the standards are dragged and dropped. The second column labeled ‘Standard type’ is where the standards are classified. Examples include ‘Thru,’ ‘Switch terms,’ ‘Line (gamma unknown),’ and ‘Reflect (S11=S22).’ The third column labeled ‘Length’ is where the ‘Parameter’ files corresponding to the standards’ lengths are placed. And the fourth column labeled ‘Measurement’ is where the uncorrected measurement files of the standards are placed. For two-port devices, the measurements can be either ‘s2p’ files for *S*-parameters or ‘w2p’ files for wave-parameters. Note that the MUF does not provide data collection from VNAs – external software is required.

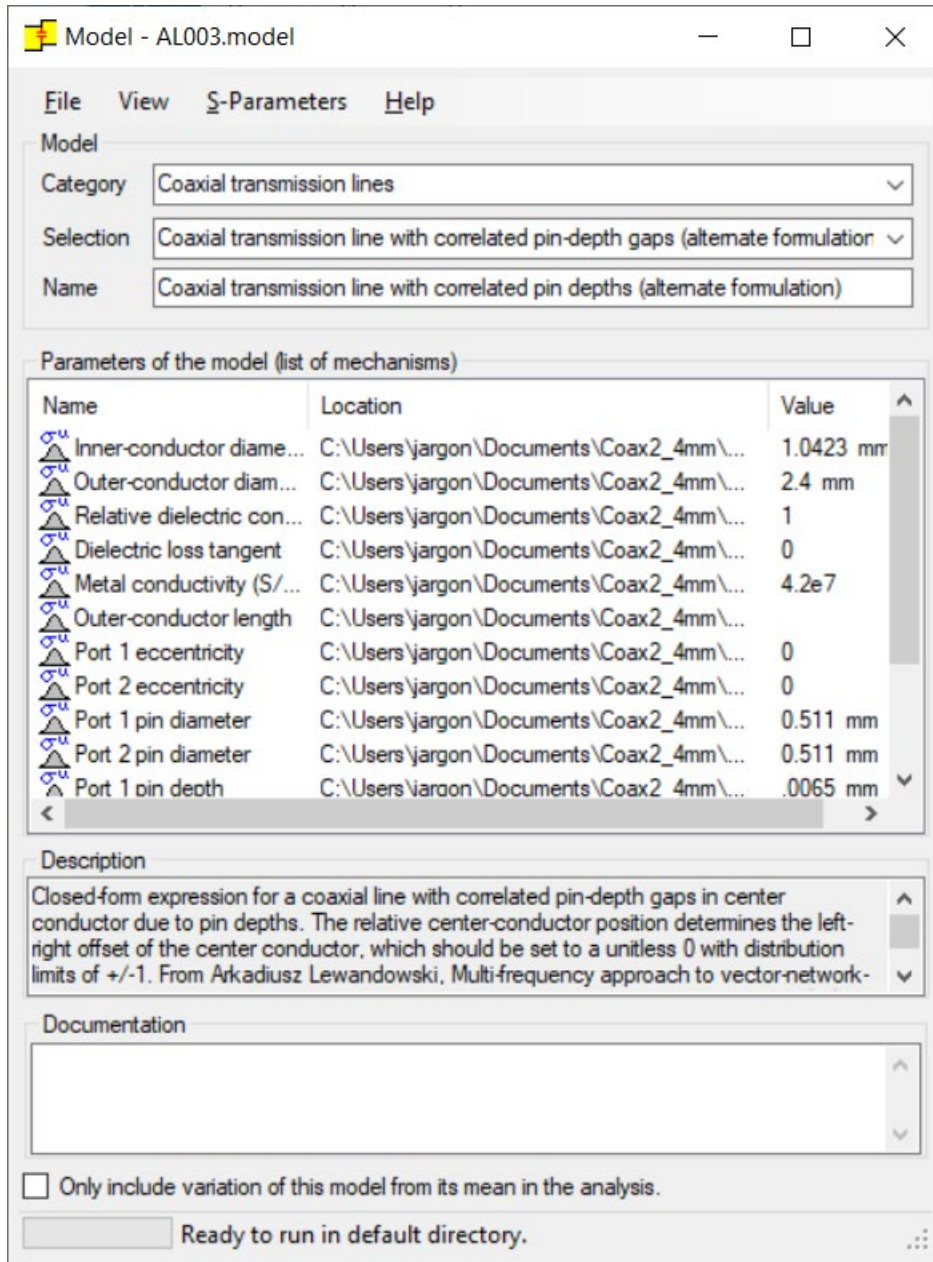


Fig. 5. MUF 'Model' file of coaxial transmission-line standard (S/N A003) with correlated pin-depth gaps. Note that the 'Length' parameter does not show a corresponding value since it is represented by a 'Sum of Parameters' file.

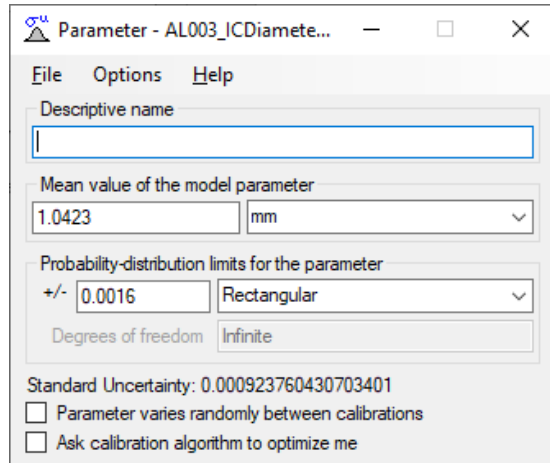


Fig. 6. MUF 'Parameter' file of transmission-line standard's inner conductor diameter (S/N A003).

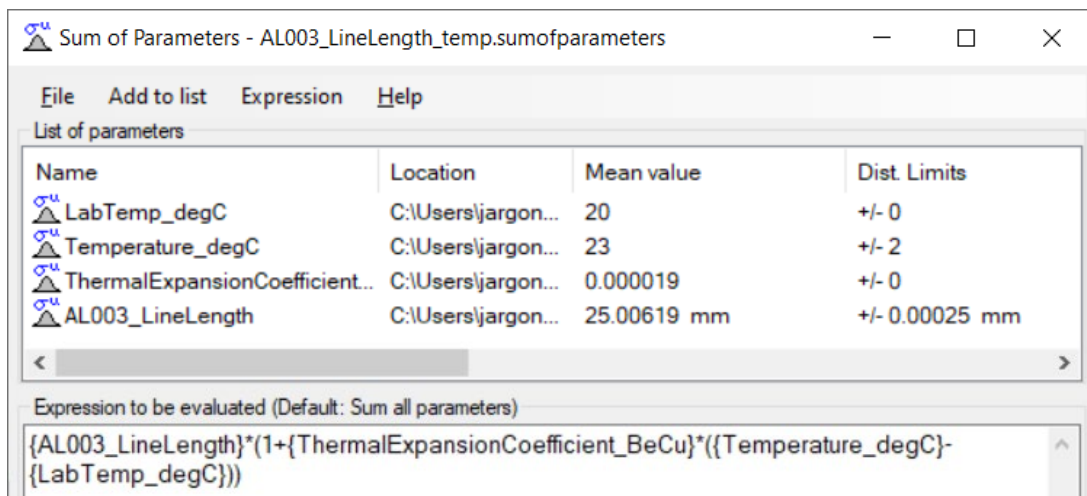


Fig. 7. MUF 'Sum of Parameters' file of transmission-line standard's length (S/N A003).

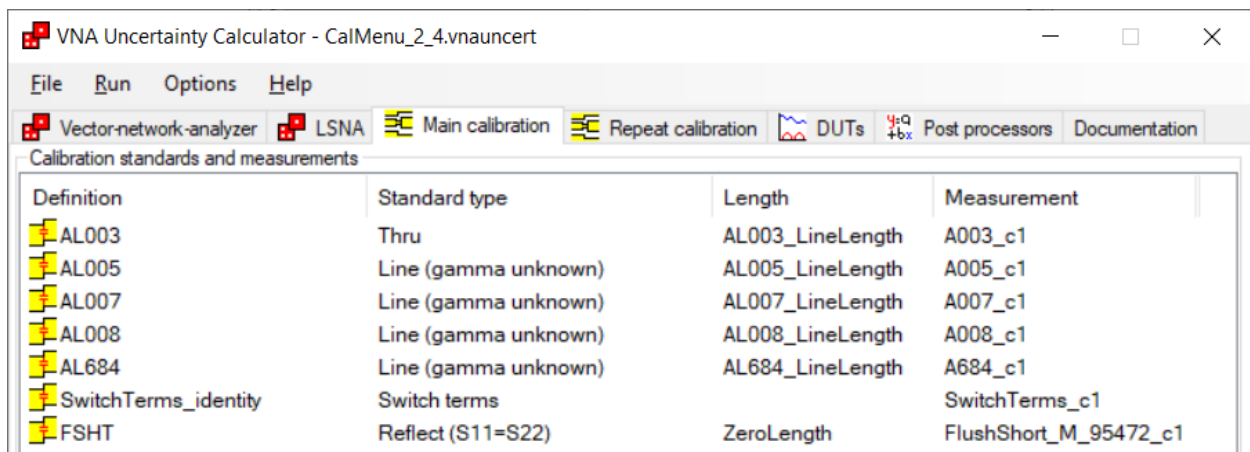


Fig. 8. MUF 'VNA Uncertainty Calculator' showing definitions, types, and measurement files.

In our example, we measured the S -parameters of several airlines and a short circuit (see Fig. 8). Airline S/N A003 was defined as the ‘thru’ standard. Since this standard has a length of 25.00619 mm, we were required to perform a reference plane translation of -12.503095 mm, where the negative sign refers to moving the reference plane toward the VNA. This was set under the ‘Options’ menu. All measurements were taken on the following frequency grid: 0.05 GHz to 0.1 GHz in steps of 0.005 GHz; 0.15 GHz to 1 GHz in steps of 0.05 GHz; and 1.1 GHz to 50 GHz in steps of 0.1 GHz. The VNA’s IF bandwidth was set to 10 Hz with no averaging [26].

Once the calibration was performed, we obtained frequency-dependent values of effective relative permittivity $\epsilon_{r,\text{eff}}$ – the real part is shown in Fig. 9 and the imaginary part is shown in Fig. 10. We used the equations presented in Section 3 to determine the metal conductivity σ , shown in Fig. 11. We calculated the mean and standard deviation of σ over all frequencies above 2 GHz (since the TRL calibration is less reliable at lower frequencies) to be $8.9 \times 10^6 \pm 0.5 \times 10^6$ S/m.

With this value plugged back into the standard models, we reran the multiline TRL calibration and corrected our DUT measurement, in this case airline (S/N A681). Fig. 12 plots the measured magnitude of S_{21} as a function of frequency as well as the values modeled by the MUF. The large discrepancies between the modeled and measured values may be explained by the airlines’ surface roughness, residual machining stresses, and multiple layers of metal. Thus, we iteratively adjusted the metal conductivity in the model and found that a value of 4.2×10^7 S/m with estimated uncertainties of $\pm 0.3 \times 10^7$ S/m resulted in much better agreement, as shown in Fig. 12.

Adjusting the conductivity value in the models of all the airlines, we reran the multiline TRL calibration once again and plotted the magnitude of S_{21} for the same airline as a function of frequency along with its 95 % confidence intervals, as shown in Fig. 13. The discrepancies between the modeled and measured values at lower frequencies (< 0.015 dB) may be attributed to the multiline TRL calibration’s limitations, where long line standards are required. Typically, calibrations utilizing lumped element standards such as opens, shorts, and loads are performed at frequencies below 2 GHz. The largest uncertainty contributions were from the temperature and the pin depths of the shortest (S/N A003) airline. We also examined the systematic uncertainties of the argument of S_{21} and discovered the total standard uncertainty was less than 0.2 degrees at all frequencies. Fig. 14 plots the magnitude of S_{11} as a function of frequency along with its 95 % confidence intervals.

Fig. 15 compares the measured values and 95% confidence intervals of $|S_{21}|$ for a 20 dB attenuator check standard (S/N C24201) (systematic uncertainties only) along with a previous measurement and its traditional associated uncertainties (systematic and random uncertainties) [3]. The measured values show agreement within their respective uncertainties. Preliminary studies indicate the overall random uncertainties are larger than the systematic components discussed in this document, which is consistent with recent studies in WR15 rectangular waveguide [27-29]. We plan to quantify random uncertainties for our 2.4 mm coaxial measurements in a future study.

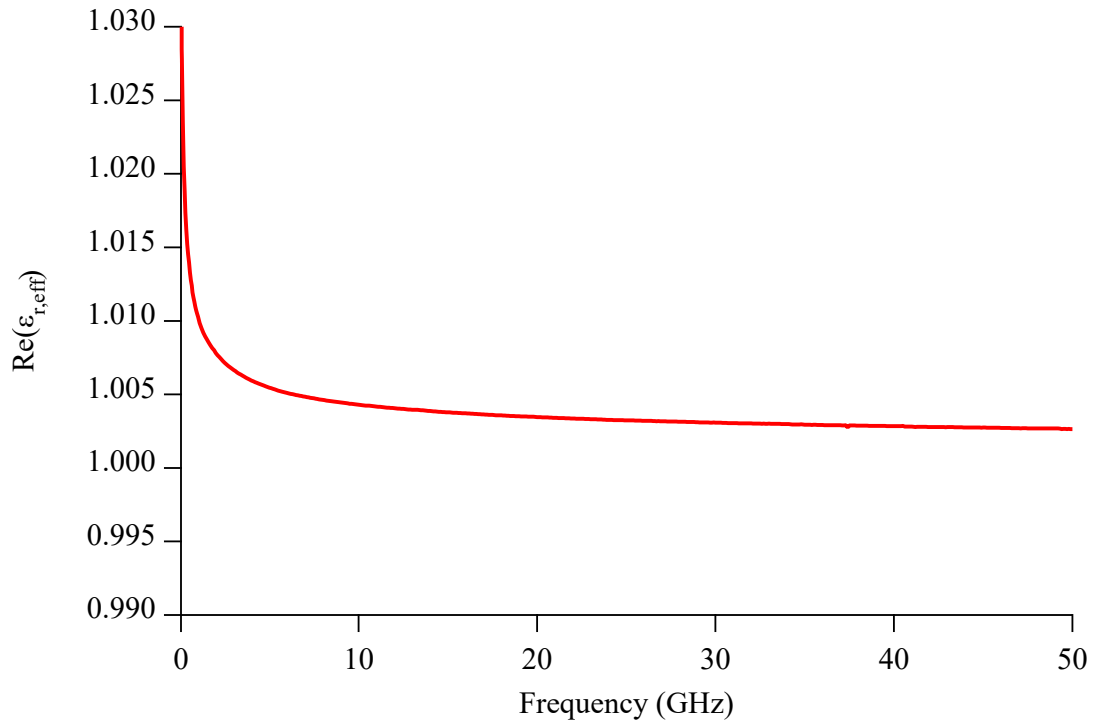


Fig. 9. Real part of $\epsilon_{r,\text{eff}}$ obtained from the multiline TRL calibration.

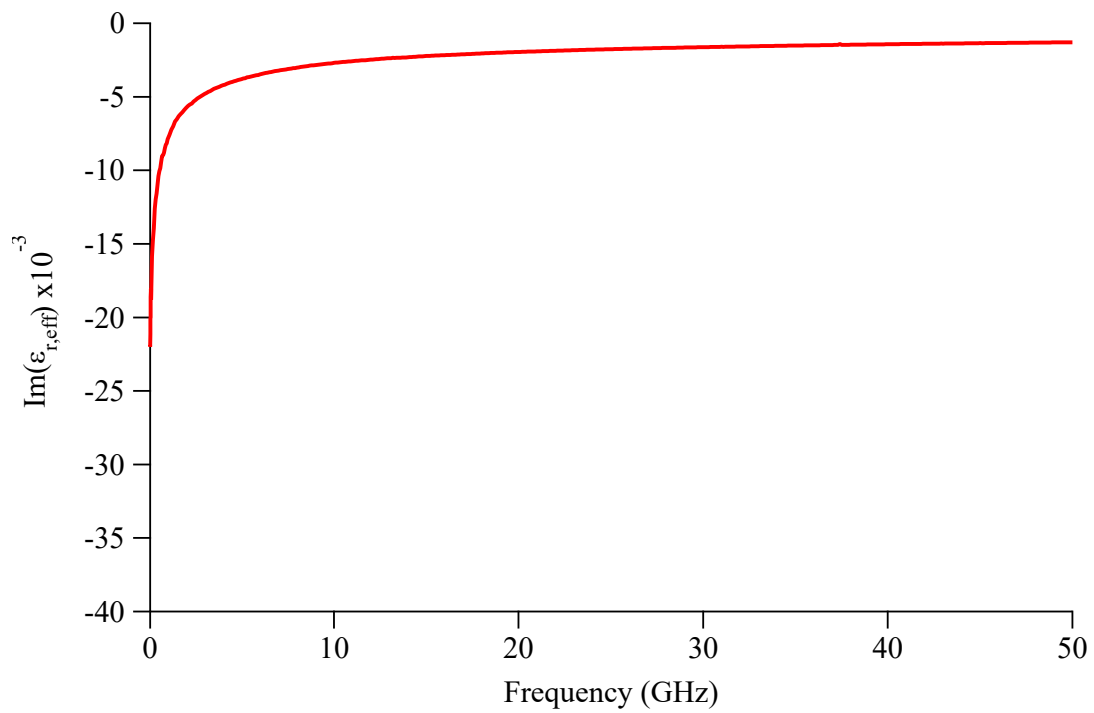


Fig. 10. Imaginary part of $\epsilon_{r,\text{eff}}$ obtained from the multiline TRL calibration.

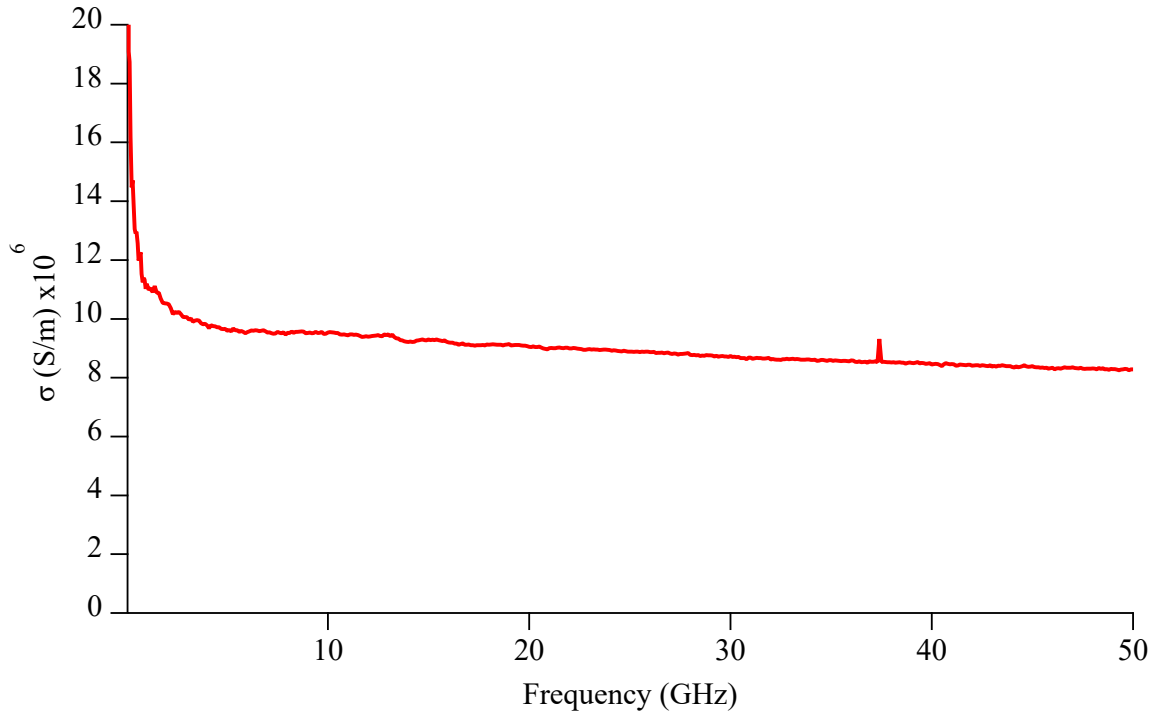


Fig. 11. Metal conductivity σ calculated using equations in Section 3.

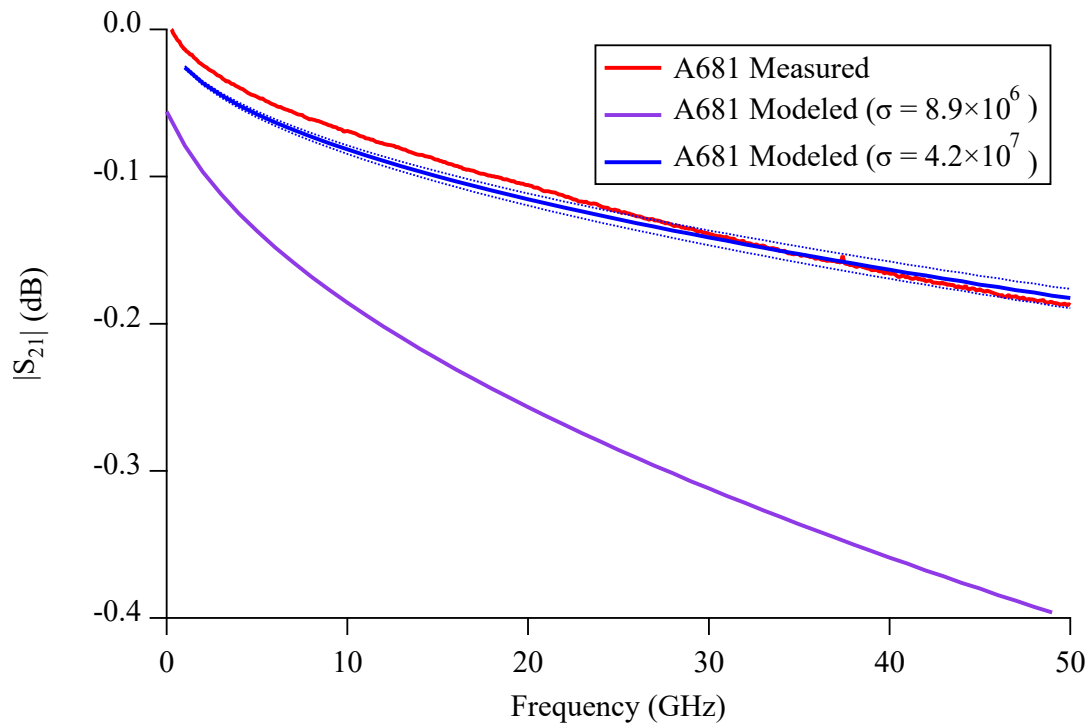


Fig. 12. Measured and modeled values ($\sigma = 8.9 \times 10^6$ S/m and $\sigma = 4.2 \times 10^7 \pm 0.3 \times 10^7$ S/m) of $|S_{21}|$ as a function of frequency for airline (S/N A681).

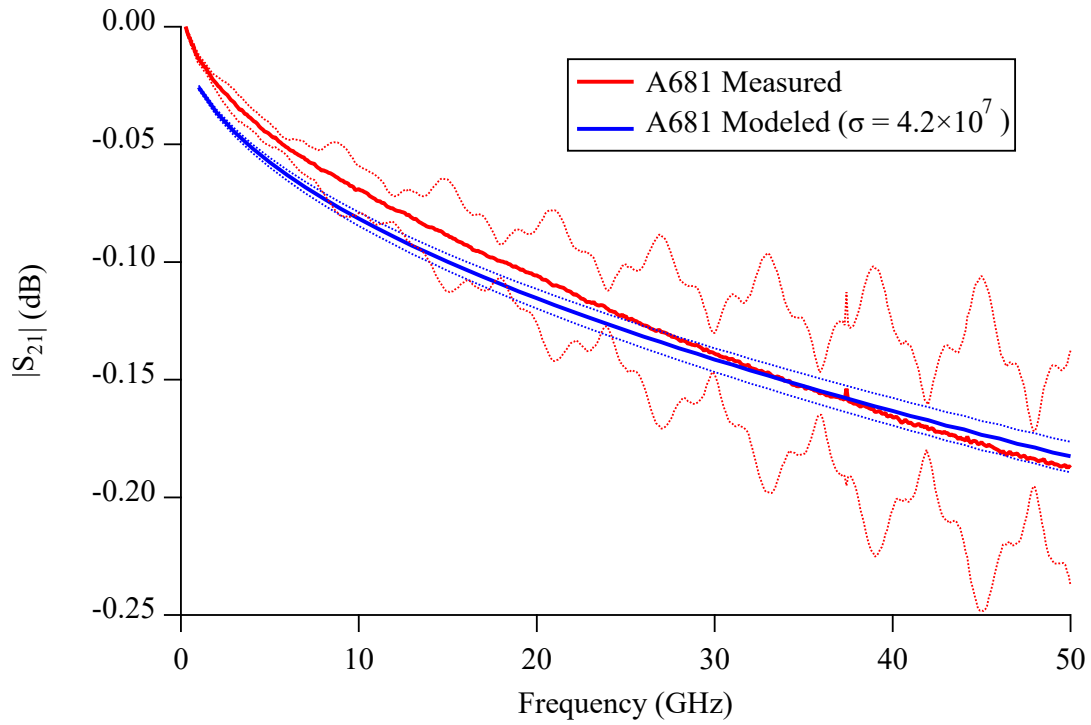


Fig. 13. Measured (with 95 % confidence interval dashed lines) and modeled values ($\sigma = 4.2 \times 10^7 \pm 0.3 \times 10^7$ S/m) of $|S_{21}|$ as a function of frequency for airline (S/N A681).

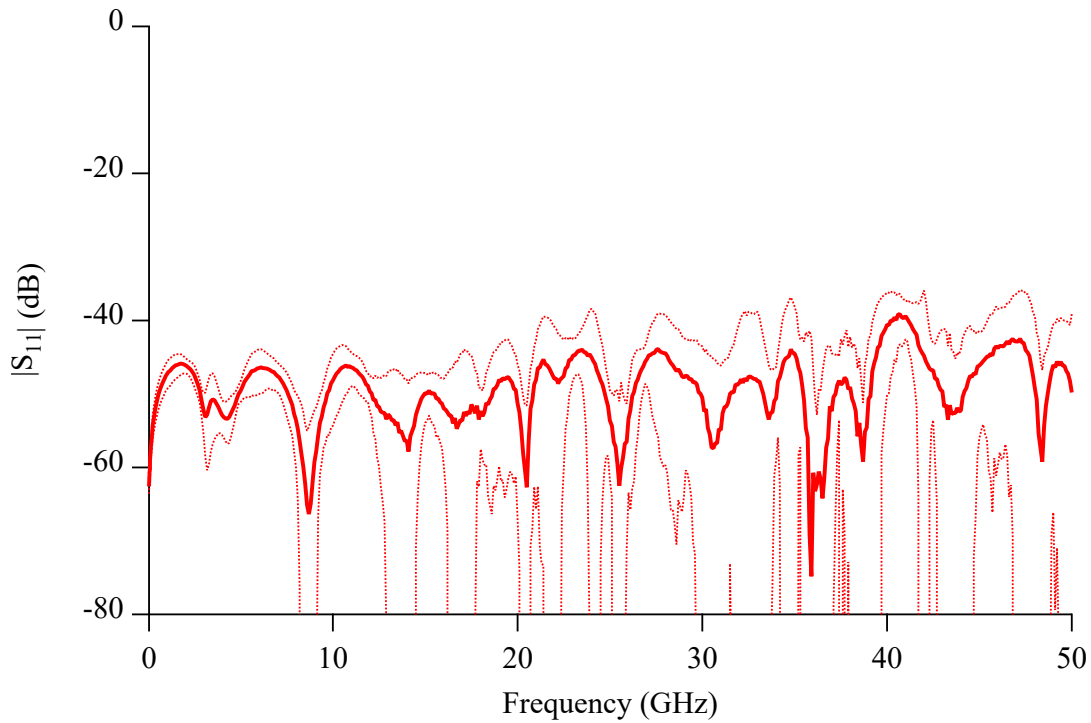


Fig. 14. Measured (with 95 % confidence interval dashed lines) of $|S_{11}|$ as a function of frequency for airline (S/N A681).

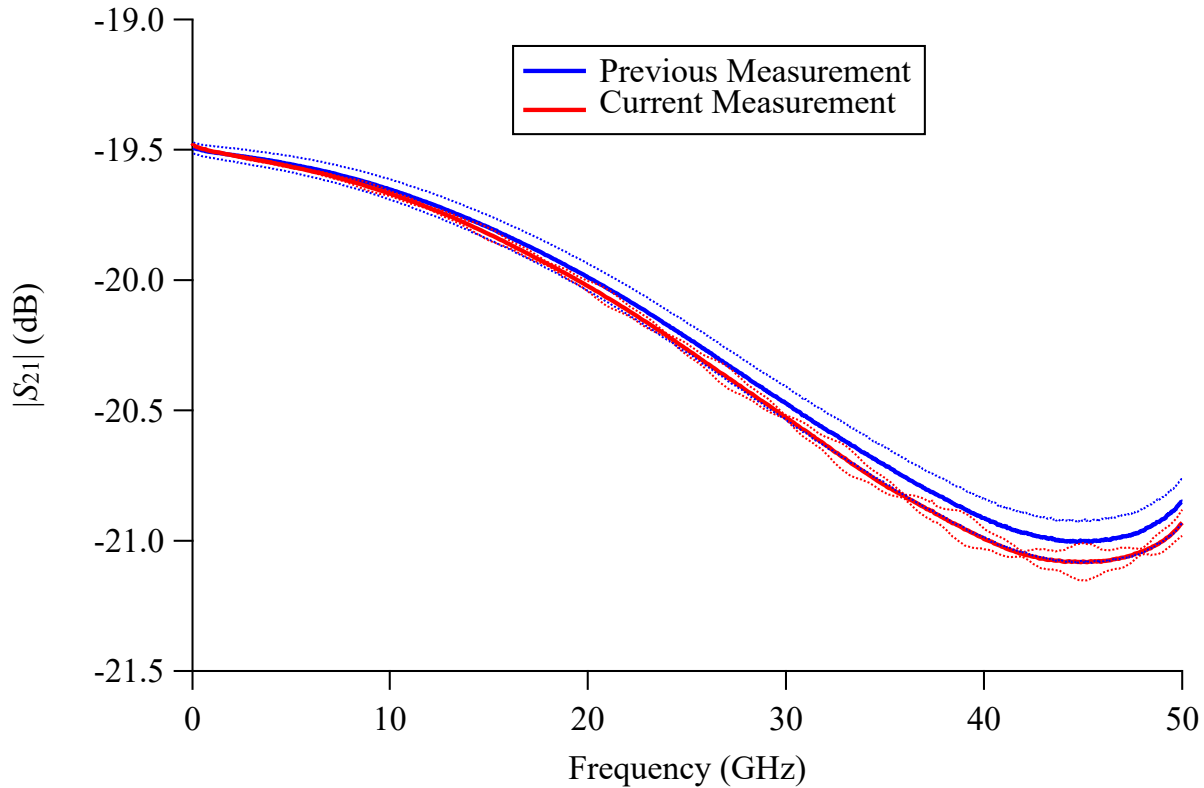


Fig. 15. Values of $|S_{21}|$ as a function of frequency along with its 95 % confidence intervals for the calibrated 20 dB attenuator check standard (S/N C24201) compared to a previous measurement along with its traditional confidence intervals.

7. Conclusions

We described the models, dimensional measurements, and internal software package for performing traceable multiline TRL calibrations up to 50 GHz using our current 2.4 mm coaxial airline standards. Our measurements of a check standard agreed to historical values within their respective uncertainties. Upcoming plans include quantifying random uncertainties of our 2.4 mm coaxial measurement system, such as noise floor, trace noise, VNA drift, VNA nonlinearity, isolation, test port cable stability, and connection repeatability.

References

- [1] NIST Mission, Vision, Core Competencies, and Core Values. Available at <https://www.nist.gov/about-nist/our-organization/mission-vision-values>.
- [2] Bureau International des Poids et Mesures (BIPM) (2012) International Vocabulary of Metrology – Basic and General Concepts and Associated Terms (VIM), Third Edition.
- [3] Special Microwave and RF Scattering-Parameter Measurement Services SKU: 61290S. Available at: <https://shop.nist.gov>.

- [4] Marks RB (1991) A multiline method of network analyzer calibration. *IEEE Transactions on Microwave Theory and Techniques*, 39 (7): 1205-1215.
- [5] Marks RB, Williams DF (1992) A general waveguide circuit theory. *Journal of Research of the National Institute of Standards and Technology*, 97 (5): 533-562.
- [6] Marks RB (1997) Formulations of the basic vector network analyzer error model including switch terms. *50th ARFTG Microwave Measurement Conference*, pp. 115-126.
- [7] Jargon JA, Williams DF, Sanders A (2018) The relationship between switch-term-corrected scattering-parameters and wave-parameters measured with a two-port vector network analyzer. *IEEE Microwave and Wireless Components Letters*, 28 (10): 951-953.
- [8] Marks RB, Williams DF (1991) Characteristic impedance determination using propagation constant measurement. *IEEE Microwave and Guided Wave Letters*, 1 (6): 141-143.
- [9] Institute of Electrical and Electronics Engineers (IEEE) (2007) Standard for Precision Coaxial Connectors (DC to 110 GHz) Standard, Standard 287.
- [10] Williams DF (2020) NIST Microwave Uncertainty Framework, Available at: <https://www.nist.gov/services-resources/software/wafer-calibration-software>.
- [11] Dimitrios J (1965) Exact cutoff frequencies of precision coax. *Microwaves*: 28-31.
- [12] Lewandowski A (2010) Multi-frequency approach to vector-network-analyzer scattering-parameter measurements. Ph.D. Thesis (Warsaw University of Technology).
- [13] Leuchtman P, Rüfenacht J (2004) On the calculation of the electrical properties of precision coaxial lines. *IEEE Trans. Instrum. Meas.*, 53 (2): 392–397.
- [14] Vacuum Magnetic Permeability, The NIST Reference on Constants, Units, and Uncertainty, Available at: <https://physics.nist.gov/cgi-bin/cuu/Value?eqmu0>.
- [15] Vacuum Electric Permittivity, The NIST Reference on Constants, Units, and Uncertainty, Available at: https://physics.nist.gov/cgi-bin/cuu/Value?ep0|search_for=permittivity.
- [16] Sladek N (1965) Fundamental considerations in the design and application of high precision coaxial connectors. *Proc. IRE International Convention Record*, 13: 182–189.
- [17] Daywitt WC (1990) First-order symmetric modes for a slightly lossy coaxial transmission line. *IEEE Trans. Microw. Theory Tech.*, 38 (11): 1644–1650.
- [18] Eiø CP, Protheroe SJ, Ridler NM (2006) Characterizing beadless air lines as reference artefacts for *S*-parameter measurements at RF and microwave frequencies. *IEE Proc.-Sci. Meas. Technol.*, 153 (6): 229-234.

- [19] MacKenzie TE, Sanderson AE, (1966) Some fundamental design principles for the development of precision coaxial standards and components. *IEEE Trans. Microw. Theory Tech.*, 14 (1): 29–39.
- [20] Kerns DM, Beatty RW (1967) *Basic Theory of Waveguide Junctions and Introductory Microwave Network Analysis* (Pergamon Press).
- [21] Special Tests of Diameter SKU: 11050S. Available at: <https://shop.nist.gov>.
- [22] Jargon JA, Arz U, Williams DF (2012) Characterizing WR-8 waveguide-to-CPW probes using two methods implemented within the NIST Uncertainty Framework. *80th ARFTG Microwave Measurement Conference*.
- [23] Jargon JA, Cho CH, Williams DF, Hale PD (2015) Physical models for 2.4 mm and 3.5 mm coaxial VNA calibration kits developed within the NIST Microwave Uncertainty Framework. *85th ARFTG Microwave Measurement Conference*.
- [24] Lewandowski A, Williams DF, Hale PD, Wang CM, Dienstfrey A (2010) Covariance-matrix-based vector-network-analyzer uncertainty analysis for time-and frequency-domain measurements. *IEEE Trans. Microwave Theory Tech.*, 58 (7): 1877-1886.
- [25] Coefficients of Linear Thermal Expansion, Available at: www.engineeringtoolbox.com.
- [26] Jargon JA, Koepke AA, Hale PD (2019) Investigating the effects of IF bandwidth and averaging on calibrated scattering-parameter measurements. *93rd ARFTG Microwave Measurement Conference*.
- [27] Jargon JA, Williams DF, Stelson AC, Long CJ, Hagerstrom AM, Hale PD, Stoup JR, Stanfield ES, Ren W (2020) Physical models and dimensional traceability of WR15 rectangular waveguide standards for determining systematic uncertainties of calibrated scattering-parameters. *NIST Technical Note 2109*.
- [28] Hagerstrom AM, Stelson AC, Jargon JA, Long CJ (2022) Quantifying noise floor and trace noise in VNA measurements for the WR-15 waveguide band. *98th ARFTG Microwave Measurement Conference*.
- [29] Stelson AC, Hagerstrom AM, Jargon JA, and Long CJ (2022) Quantifying receiver nonlinearities in VNA measurements for the WR-15 waveguide band. *IEEE Trans. Microwave Theory Tech.*, 70 (5): 2743-2749.